J Mater Sci (2008) 43:2912–2921
DOI 10.1007/s10853-007-1803-7

Creep behavior of INCOLOY alloy 617

Marcello Cabibbo · Elisabetta Gariboldi · Stefano Spigarelli · Dario Ripamonti

Received: 2 May 2006 / Accepted: 24 April 2007 / Published online: 3 July 2007

Abstract The microstructural features of INCOLOY alloy 617 in the solution annealed condition and after long-term creep tests at 700 and 800 °C were characterized and correlated with hardness and creep strength. Major precipitates included $(Cr,Mo,Fe)_{23}C_6$ carbides and the δ-Ni_3Mo phase. M_6C and MC carbides were also detected within the austenitic grains. However, minor precipitates particularly γ'-$Ni_3(Al,Ti)$ was found to play an important role. At different exposure temperatures, the microstructural features of the Ni–22Cr–12Co–9Mo alloy changed compared with the as-received condition. The presence of discontinuously precipitated $(Cr,Mo,Fe)_{23}C_6$ carbides and their coarsening until the formation of an intergranular film morphology could be responsible both for a reduction in rupture strength and for enhanced intergranular embrittlement. The fraction and morphology of the γ'-phase, precipitated during exposure to high temperature, also changed after 700 or 800 °C exposure. At the latter test temperature, a lower volume fraction of coarsened and more cubic γ' precipitates were observed. These microstructural modifications, together with the presence of the δ-phase, detected only in specimens exposed to 700 °C, were clearly responsible for the substantially good creep response observed at 700 °C, compared with that found at 800 °C.

M. Cabibbo (✉) · S. Spigarelli
Dipartimento di Meccanica, Università Politecnica delle Marche,
Via Brecce Bianche, Ancona 60131, Italy
e-mail: m.cabibbo@univpm.it

E. Gariboldi · D. Ripamonti
Dipartimento di Meccanica, Politecnico di Milano,
Via La Masa 34, Milano, Italy

Introduction

The Ni–22Cr–12Co–9Mo alloy (also known as INCOLOY 617®) is used throughout the world for high-temperature applications. It is also one of the materials proposed for some of the most ambitious EU and US projects for future generations of power plants where steam inlet temperatures might reach and even exceed 700 °C [1, 2].

The processing behavior of this type of alloy (i.e., castability, forgeability, weldability, etc.) is of primary importance for manufacturing the large-size components typical of the power plant industry. In general, severe shortcomings concerning rotor applications in high-temperature steam turbines have been noticed in all three types of superalloy, according to the accepted classification (γ'-, solid solution, γ''-strengthening classes) [3, 4]. In fact, the production of large components is hampered by the relatively high-flow strength at typical forging temperatures. On the other hand, high-standard mechanical properties (for example creep resistance) are another fundamental requirement for these alloys, for which long-term high-temperature microstructural stability is also needed.

The Ni–22Cr–12Co–9Mo alloy belongs to the group of alloys usually referred to as solid-solution strengthened (but also as carbide-hardened) materials [5, 6]. It contains molybdenum or tungsten as well as some carbon for additional carbide strengthening and is generally used in the solution-annealed condition. The mechanical properties of this alloy, like those of other superalloys, are strongly influenced by microstructural features at the normal operating temperature and may possibly be modified during service at high temperatures. Thus, a clear understanding of the role played by secondary phases is essential for a correct explanation of the long-term properties of the material [7–11].

The Ni–22Cr–12Co–9Mo alloy has been shown to exhibit a strengthening response during extended exposure to intermediate temperatures (i.e., 700–800 °C) [12]. Following heat treatment, the microstructure of the alloy is characterized by the presence of a series of precipitates both at grain boundaries and inside the grains. The effect of high-temperature exposure has been reported as enhancing the discontinuous precipitation of carbides, nitrides and carbo-nitrides, such as $M_{23}C_6$, TiN, and TiCN, at grain boundaries [3, 13]. Some particles also precipitate along and inside twins [3, 13–15]. By increasing the temperature from 700 to 900 °C, the amount of precipitates, both inside the grains and at grain boundaries, has been found to increase [13–15]. In fact, at ~700 °C both TiN, TiCN, and $M_{23}C_6$ tend to remain small and stable because of the rather slow diffusion rate of Ti and the other heavy elements. Exposure to much higher temperatures (1,000–1,100 °C) results in a lower amount of relatively coarse precipitates [13, 15]. Among the particles observed in the alloy, CrMo(C,N) carbo-nitrides have been revealed by X-ray diffraction studies but not by TEM inspections, indicating that they are rather rare particles within the microstructure [13]. Triangular-shaped particles identified as MC carbides have also been observed while other small particles of polyhedral shape, have been identified as TiN [16, 17]. $M_{23}C_6$ carbides, appearing as polyhedral particles [16], characterize Ni–22Cr–12Co–9Mo alloy microstructure within the temperature range 700–1,100°C. Finally, exposure at ~700 °C (especially during creep) has also been shown to form a network of acicular δ-phase (orthorhombic intermetallic Ni_3Nb phase), bridging grain boundaries and extending across grains [18]. The latter phase has been reported as forming directly from the supersaturated solid solution during aging at relatively high temperatures. The precipitation of the δ-Ni_3Mo phase initiates in the Nb and Mo enriched regions of grain and twin boundaries and matrix carbides [19–23]. Precipitation of the δ-phase in Inconel 625 has been reported as very rapid at temperatures above 800 °C [22, 23], its solvus temperature being ~1,010 °C with a sub-solvus temperature of ~950 °C [24]. The δ-phase is incoherent and it weakly contributes to alloy strengthening, although it is desirable for grain size control during the processing and heat treatment of the wrought alloy [25–28]. The presence of the δ-phase at grain boundaries has been reported as beneficial for enhanced ductility and toughness [21–23, 29, 30]. In fact, some authors [19, 20, 31] have shown that the presence of the δ phase among other particles (both carbides and nitrides) within the microstructure does not significantly impair the toughness of the alloy, and, in some cases, may provide a barrier to grain boundary sliding during creep by pinning the boundaries. On the other hand, the laths of δ extending across grains appear to grow to the detriment of the strengthening γ' precipitates.

The γ' phase is a typical strengthening phase in many Ni-base superalloys with high Ti/Al ratios. It is usually in the form Ni_3Ti or $Ni_3(Al,Ti)$ [26, 27]. This phase has also been found in small amounts in the Ni–22Cr–12Co–9Mo alloy exposed to a temperature range of 650–760 °C [3, 13]. However, no trace of it has been found after prolonged exposure to 816 °C [13] or after 2 h exposure to 800 °C. Therefore, the solvus temperature of the γ' phase could reasonably lie in the temperature range of between 760 and 800 °C.

This paper focuses on microstructural changes, and particularly on precipitation phenomena, occurring in Ni–22Cr–12Co–9Mo alloy during exposure to temperatures of 700 and 800 °C in loaded and unloaded aged specimens.

Material and experimental procedures

The investigated material was an NiCr22O12Mo alloy (UNS N006617, Wr.N. 2.4663, that can also be referred to by its trade name, INCOLOY 617®), with the chemical composition shown in Table 1. The material was supplied by Krupp VDM as 12 mm thick plate, which was hot worked, solution treated at 1,180°C for 32 min and water quenched. The material was creep tested by a consortium of Italian Laboratories at temperatures of 700 and 800 °C [12]. These temperatures were chosen as they are, respectively, the hardening and softening reference temperatures for the investigated alloy. The results of the creep tests are presented in [12]. Details of temperatures and exposure times are reported in Table 2 of this paper together with the specimen reference codes.

Metallographic inspections were carried out on the load-free and load-bearing regions of selected specimens (gripping ends and gauge length, respectively) using optical microscopy (OM), scanning electron microscopy (SEM), and transmission electron microscopy (TEM) techniques in order to characterize the presence of the secondary hardening phases. Metallographic samples for

Table 1 Chemical composition of the investigated 617 alloy (mass %)

Cr	Ni	Mn	Si	Mo	Ti	Fe	S	P	Al	Co	B	C
21.60	54.05	0.09	0.08	9.05	0.37	1.54	0.002	0.004	1.190	11.60	0.001	0.078

Table 2 Reference codes and general information about creep tested and microstructurally characterized materials: creep test temperature (T) and duration (t), specimen elongation (EL) and reduction in area (RA); Vickers (HV) and Rockwell C (HRC) hardness measured on the load-free gripping ends of the creep specimens

Reference code	T (°C)	t (h)	Hardness* (HV)	Hardness (HRC)
B[a]	–	–	166	7
7C	700	~34,000	262	26
8C	800	~13,000	208	13

[a] Base metal, taken from a specimen not subjected to creep test

* Hardness measurements (HV and HRC) within an error of 1%

OM and SEM were longitudinally and transversally sectioned from crept specimens using a diamond saw cutting device, mounted in phenolic resin and polished. Depending on the microstructural condition, specimens were etched using either a solution of 15 mL HCl, 10 mL CH_3COOH, 10 mL HNO_3 (*Aqua regia*) or 30 mL HCl and 10 mL HNO_3. Energy dispersive spectrum (EDS) microanalyses were performed in an SEM by means of an Oxford Inca Energy® 200 system. Films for TEM observations were mechanically ground to 200 μm and chemically etched using a solution of 10 mL HNO_3 and 90 mL methyl alcohol. Discs were punched and finally thinned by twin-jet electropolishing (Tenupol®-5) using a solution of 10 mL HCl_4 and 90 mL methyl alcohol at 22 V and $T = -50$ °C. A Philips® CM200 microscope, equipped with a double tilt specimen holder, was used. The vast majority of the phase identifications were performed using the convergent beam (CB) selected area electron diffraction pattern (SAEDP).

Vickers micro-hardness (981 N load on the indenter) was measured on the load-free regions of crept specimens (specimens 7C and 8C), and on the as-received material (specimen B). In addition to specimens used for metallographic investigations, macro-hardness tests were performed on other selected specimens exposed to the two investigated temperatures. In order to compare results with literature data [11], Rockwell C hardness (HRC) tests were also performed on the same specimens.

Results

As-received material

The typical metallographic features of the investigated material in the as-received condition (specimen B) are shown in Fig. 1. The presence of a banded structure is clearly visible (1(a)). The bands are characterized by fine austenitic grains and by a significant presence of secondary phases.

The secondary phases observed with OM and SEM images were of two types. A first type of particle, which

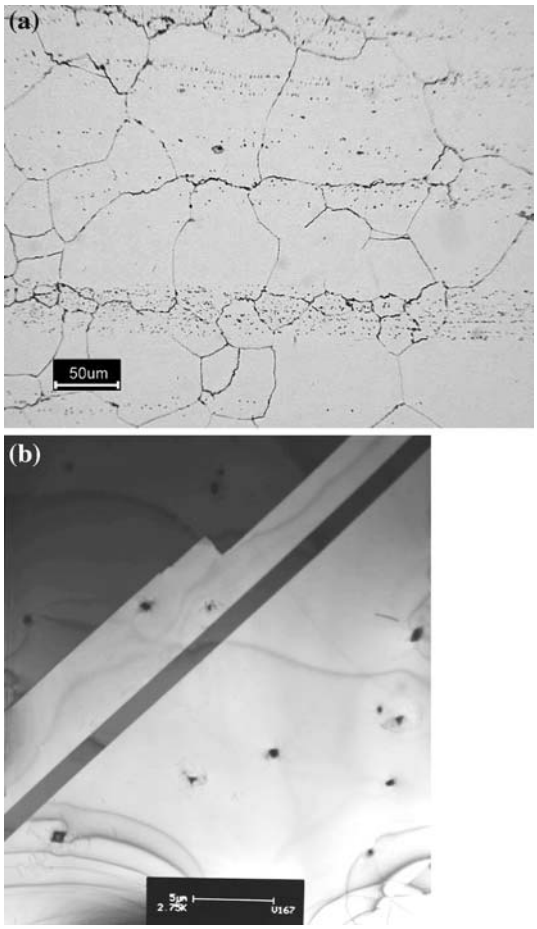

Fig. 1 (**a**) Typical metallographic features (OM) of the as-received material (longitudinal section); (**b**) low-magnification TEM image showing a clear grained austenitic structure with straight and parallel twins. A few intragranular carbides are also visible

was relatively rare and homogeneously distributed, was light orange in OM micrographs. These particles, also visible on un-etched samples, had diameters in the range of 4–10 μm. Microanalyses showed that they were rich in Ti, C and N, and are therefore probably titanium carbo-nitrides Ti(C,N). The other set of particles lay along the banded structure. These particles were blocky-shaped, situated at inter- and intra-granular sites, and with a mean size of 0.2–1 μm. EDS analyses on the particles showed that they contained Cr and Mo. No trace of other hardening phases was found by OM and SEM. Figure 2 is a plot graph summarizing the EDS analyses, where the composition of several particles is plotted against their content in Ni. Since carbon was also observed within the particles, they were probably $(Cr,Mo)_{23}C_6$ carbides.

TEM images showed a plain grain structure interrupted only by rather straight and long twins bridging the whole grains from side to side (as shown in Fig. 1b). The as-received material is characterized by a limited amount of carbides both along grain boundaries and within grain

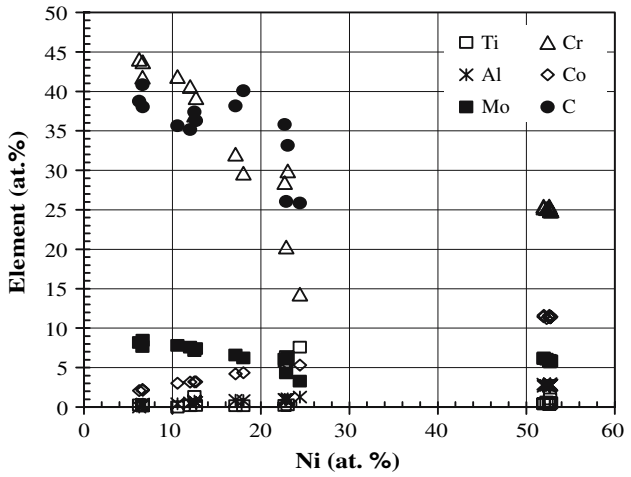

Fig. 2 Chemical composition of the precipitates found within the banded structure in specimen B. The data are plotted as a function of the Ni content

cores. Carbide identification using CB-SAEDP showed that the vast majority of these carbides were of the $M_{23}C_6$ type, with M being essentially Cr, Mo, Fe ($(Cr,Mo,Fe)_{23}C_6$). This form of carbide has a complex cubic lattice with 92 metal atoms (Cr, Mo, Fe) and 24 carbon atoms per unit cell [22, 23]. In addition to $M_{23}C_6$ carbides, MC ((Cr,Mo,Fe)C) and M_6C ($(Cr,Mo,Fe)_6C$) carbides were also detected in isolated cases.

In summary, the microstructural analyses revealed that, in the as-received condition, the $(Cr,Mo,Fe)_{23}C_6$ carbides constituted the predominant population of particles in the investigated alloy.

Material creep tested at 700 °C

The microstructure of the alloy held at 700 °C for about 3.4×10^4 h (specimen 7C) is shown in Fig. 3 (OM and SEM) and Fig. 4 (TEM). With OM the microstructure still showed a banded structure similar to the as-received material (Fig. 3a). Rare and homogeneously distributed Ti(C,N) and $(Cr,Mo,Fe)_{23}C_6$ carbide particles were also observed in this specimen (Fig. 3b). A feature that distinguished specimen 7C from specimen B was the presence of two additional types of particles, observed both inside and outside the fine-grained bands. The first type of particle, that appeared similar to $(Cr,Mo,Fe)_{23}C_6$ carbides using OM, merely decorated grain boundaries. A second type of fine and elongated particle, darker with OM, was located not only at grain boundaries but also along twin boundaries. The SE-SEM images revealed grain boundaries significantly decorated with at least two distinct phases (Fig. 3c). EDS measurements, acquired from the bright particles, revealed that they were rich in Mo.

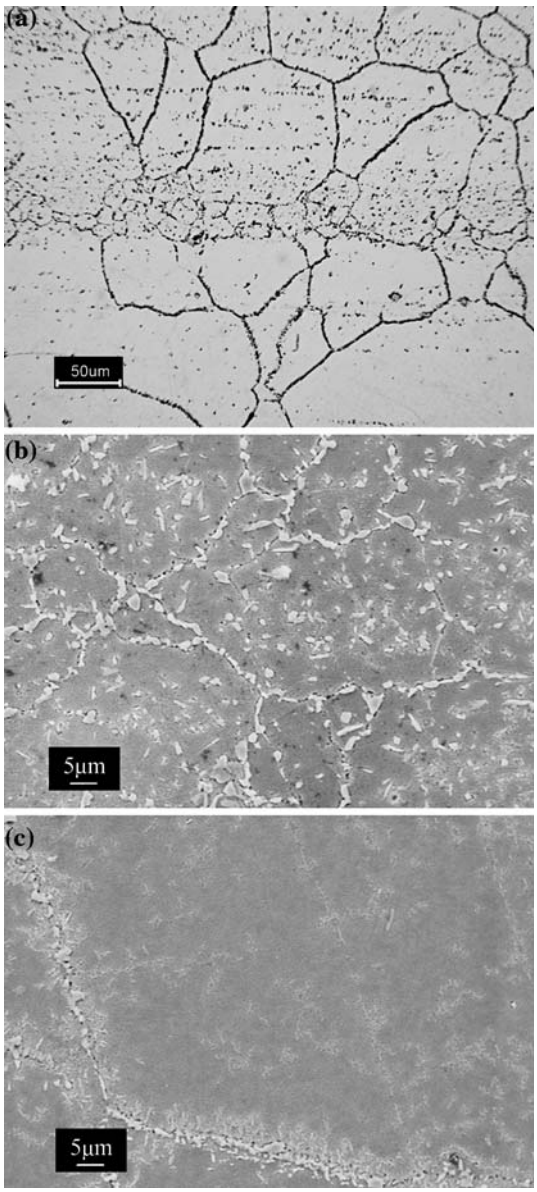

Fig. 3 Specimen 7C. Typical metallographic microstructure (OM): (**a**) SEM, secondary electron images showing grain boundary and intragranular carbides and (**b**) a detail of a grain boundary decorated with $(Cr,Mo,Fe)_{23}C_6$ carbides from which a series of almost parallel strips of plate-like alternating δ-Ni_3Mo phase proceeds inwards

TEM inspections at a far greater magnification level on the load-bearing region of the specimen revealed another interesting feature which distinguishes specimen 7C from specimen B: the appearance of a small but significant fraction of γ'-$Ni_3(Al,Ti)$, surrounded by dislocations. The γ' particles were spherical with a diameter of about 60 nm. In addition, a depleted zone of γ was detected at the grain boundary (Fig. 4a). The γ-matrix and γ–γ' interfaces appeared relatively free of dislocations (Fig. 4b). TEM inspections also revealed a lath-shaped δ-Ni_3Mo phase extending from grain boundaries and twin boundaries into

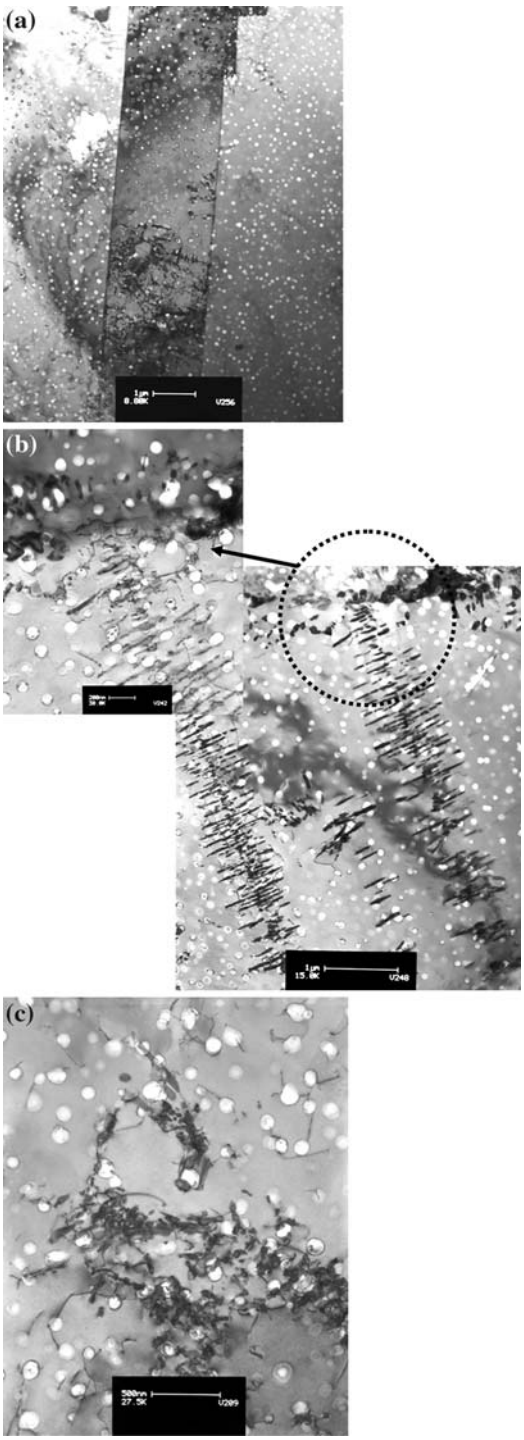

Fig. 4 Specimen 7C. TEM, bright-field images showing two twin boundaries crossing a grain: (**a**) γ' phase nucleation can be seen within the twin as well as along twin boundaries, both on incoherent and on semi-coherent twin boundaries (in the figure, the horizontal segments of the twin boundary); (**b**) shows a micrograph with the δ-phase starting from the grain boundary and advancing inwards in straight zip-like lines which are almost parallel to each other; (**c**) illustrates the γ'-phase hardening effect on the microstructure, through tangled sliding dislocations impinged by the γ' particles

the matrix, following a zip-like path. In some cases, the growth of this phase started from existing carbides. The identification of the δ-Ni_3Mo phase was carried out using the TEM–SAEDP technique. More specifically, the δ-phase, with a plate-like morphology, is the principal cause of the sometimes observed grain boundary waviness. TEM inspection showed that the growth of lath particles occurred to the detriment of γ', as there is a γ'-depleted region around the lath phase (Fig. 4c). Since most Ni is consumed in the process of δ-phase formation, the γ'-phase can only form at a certain distance from the δ-phase surroundings, where Ni is still available.

In addition to the presence of γ and δ phases, specimen 7C showed grain boundaries which were not only decorated with $M_{23}C_6$, but also with other carbides, such as MC and M_6C, this second being less abundant than the MC carbide. Prolonged exposure to 700 °C led to a considerable increase in the overall carbide population, especially at the grain boundaries and within the twins, compared with specimen B. Isolated M(C,N) carbo-nitrides of the type Ti(C,N) and (Nb,Ti)C were also observed in specimen 7C (Fig. 4c). Finally, in specimen 7C, dislocations were evenly distributed in well-defined coarse cells.

With SAEDP (Fig. 5) three different patterns are easily recognized. They can be attributed to γ (a_0 = 3.55 Å), γ' (a_0 = 3.53 Å), and $M_{23}C_6$ (a_0 = 10.80 Å) [25]. SAEDP clearly showed super-lattice spots coming from the plate-like, or square-shaped, γ'-$Ni_3(Al,Ti)$ with an average edge length of 60 nm, denoting a semi-coherency with the γ-matrix.

Material creep tested at 800 °C

The analyses of the material exposed to 800 °C (specimen 8C) were focused on the specimen held for about 13,000 h at this temperature. Both in the load-bearing and load-free regions of the crept specimen, the microstructure revealed by OM and SEM inspection was characterized by the presence of a great amount of intragranular elongated precipitates distributed in lines, probably related to specific crystallographic orientations. Two types of particles at grain boundaries were visible in SEM micrographs (Fig. 6a). The first type, dark in SEM micrographs, proved to be rich in Cr and C, while the second type of particle (bright, in Fig. 6a), mainly located in the intergranular region of the finer-grained bands, were rich in Mo and C.

In this specimen TEM images again showed the presence of the γ' phase in a reduced volume fraction compared with specimen 7C (compare Figs. 6b and 4c). Furthermore, γ' particles in specimen 8C were relatively coarse (about 255 nm in diameter) and cubic.

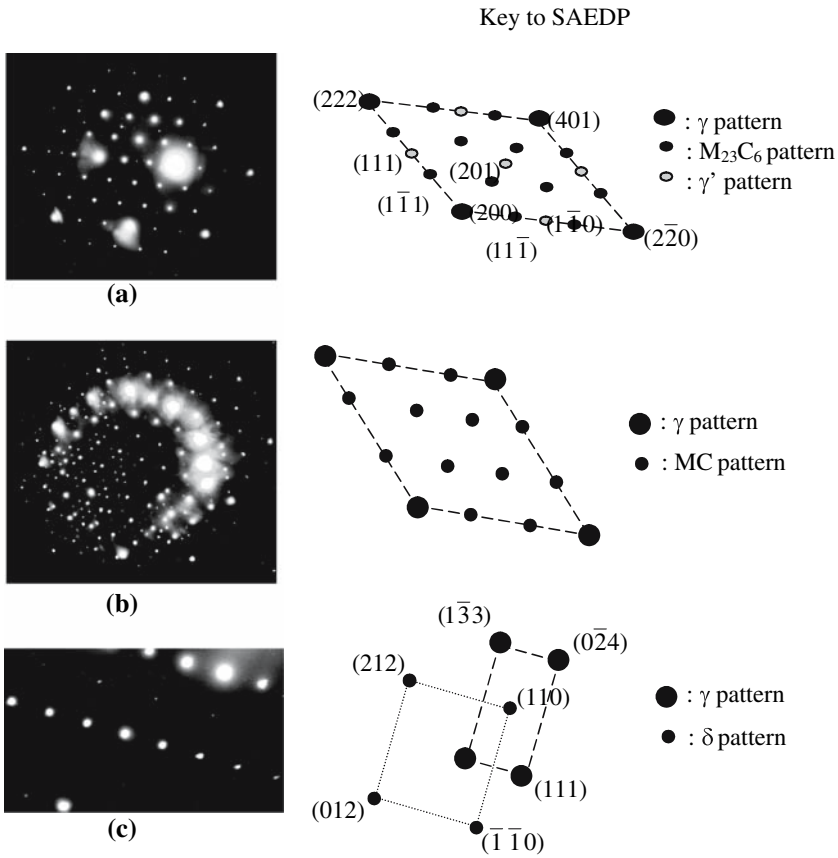

Fig. 5 Phase identification through SAEDP and related morphologies. SAEDP showing acting crystallographic planes from matrix γ, from the γ' phase, $Ni_3(Al,Ti)$, and from carbide $M_{23}C_6$, where M = Cr,Co,Ni,Mo. (**a**) SAEDP showing acting crystallographic planes from matrix γ, and carbide MC, where M = Cr,Mo; (**b**) SAEDP showing acting crystallographic planes from matrix γ and from the δ phase, Ni_3Mo

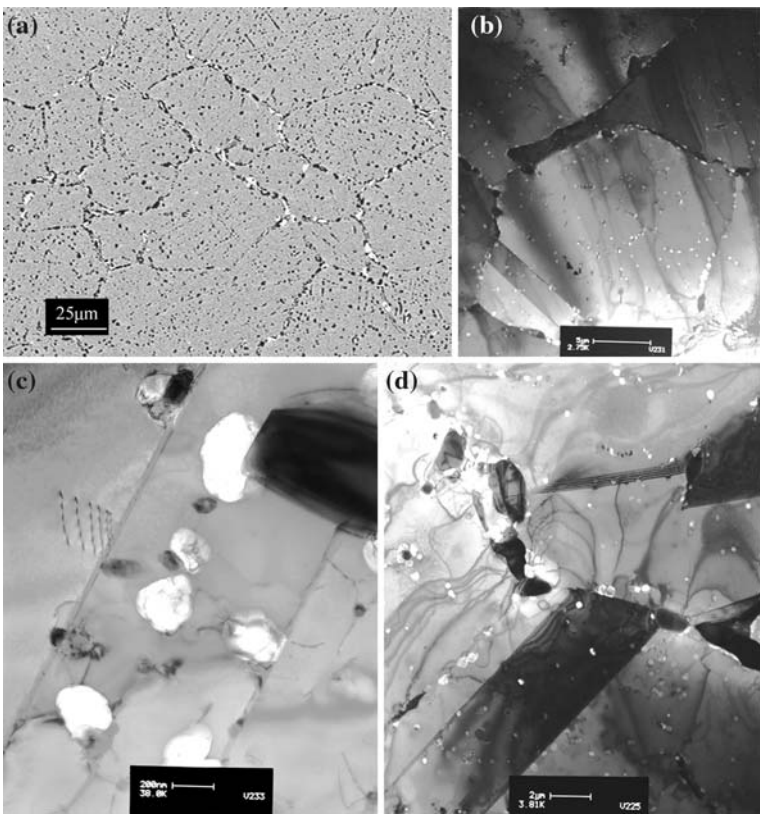

Fig. 6 Specimen 8C. (**a**) SEM image showing both intra- and intergranular particles; (**b–c**) TEM images showing the lower fraction of γ' particles with some intergranular needle-like carbides; (**d**) TEM image showing needle-like carbides and γ' inside and at the twin boundaries

Hardness measurements

The plot graph of hardness as a function of creep duration, measured at the gripping ends of the crept specimens is reported in Fig. 7. In this graph, the HRC values were plotted even when lower than 20 (the standard minimum value for valid measurements) in order to compare them with the values reported in literature for the same alloy at roughly corresponding test temperatures [32]. Data points plotted in Fig. 7 clearly show that exposure for 10^4 h was not enough to reach peak hardness values at the lowest investigated temperatures of 593 and 648 °C. At about 700 °C, hardness increased rapidly compared with lower temperatures. The curve corresponding to exposure to 760 °C shows a wide peak region starting from 10^3 to 4×10^3 h, after which material overaging was evident. The material exposed to 800 °C passed its peak value at about 10^3 h. All the curves in Fig. 7 show that the experimental creep rupture times occurred in the overaging stage.

Due to the inhomogeneous microstructure observed in the as-received (B) and aged/crept conditions (specimens 7C and 8C), micro-hardness tests were also carried out to measure this property in regions where there were different microstructural features. The micro-hardness of specimen B in the coarse grain region, when depleted of secondary phase particles, averaged at 189 HV. Hardness was higher within the bands where precipitates were observed, reaching an average value of 199 HV. Correspondingly, the micro-hardness values of specimen 7C ranged from 280 to 290 HV outside the bands, in regions where second phases were relatively rare, and increased within the bands, ranging between 300 and 310 HV, particularly when the indentation load was applied in the small grain region. Finally, the micro-hardness of specimen 8C ranged between 222 and 263 HV. In agreement with the HRC measurements, the increase in micro-hardness with respect to the as-received condition is not as marked as for material exposed to 700 °C. A slight increase in micro-hardness, when moving from the core to the external surface of crept specimen 8C, was also observed.

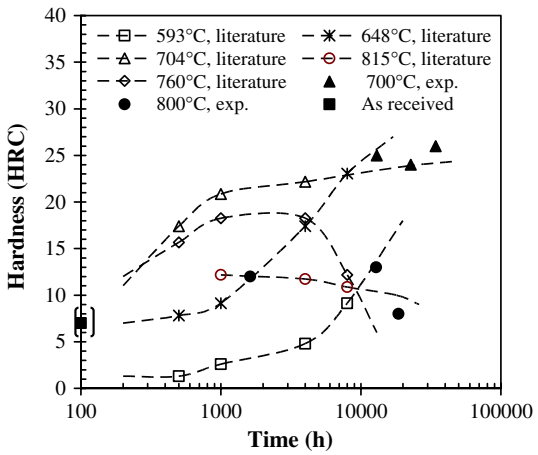

Fig. 7 HRC plotted as a function of creep duration for different specimens creep tested at 700 °C (exp. 700 °C, *solid upward triangular* symbols in the diagram) and 800 °C (exp. 800 °C, *solid circle* symbol in the diagram). The hardness value in the as-received condition (exp. as-received, *solid square* datapoints) is plotted at $t = 100$ h. Hardness measurements made on the same alloy and creep tested at 593 °C (*open square* symbol), 704 °C (*open upward triangle* datapoints), 740 °C (*open diamond* symbol), 815 °C (*open circle symbol*) by Mankins et al. [11], are also plotted for comparison

Discussion

Microstructure

The microstructural modification and the hardness of the Ni–22Cr–12Co–9Mo alloy, subjected to long-term creep tests at 700 and 800 °C for different periods of time were characterized. The main features identified were the grain boundary particle population (both $(Cr,Mo,Fe)_{23}C_6$ carbides and the δ-Ni_3Mo phase) and other types of carbides, such as M_6C and MC, that were also detected within the austenitic grains. Moreover, the precipitation and coalescence of the γ'-$Ni_3(Al,Ti)$ phase clearly played an important role in the creep response of the alloy (see also [33]).

Discontinuously precipitated carbides were observed at grain and twin boundaries. It is well-known that the discrete and discontinuous distribution of grain-boundary carbides improves the mechanical properties of the material, in particular creep resistance, since these particles effectively pin the grain boundaries, thereby decreasing the grain boundary sliding which the material is sensitive to at typical creep temperature exposures [29, 34–36]. Nevertheless, it should be pointed out that these carbides can adversely affect strain distribution, creep life, and material ductility when forming a continuous network along grain boundaries.

As far as the intragranular carbides are concerned, Lewis et al. [16] have suggested that most precipitates within the grain nucleate preferentially on dislocations, generated by the growth of the same nucleating particles. For this reason, carbides continue to grow as the material is exposed to creep temperature and load.

Reasons for nucleation on grain boundaries and dislocations may be two-fold: (i) segregation of the constituent atoms of $M_{23}C_6$ on boundaries and dislocations; (ii) reduction in the strain-energy for nucleation in regions of localized strain. The origin of this effect has generally been ascribed to the differential thermal contraction of particle and matrix. A particle growing uniformly in a matrix of smaller atomic volume would experience a similar hydro-

static compression. This particle-matrix misfit may be accommodated by the diffusion of vacancies to the growing interface. An alternative mechanism for the relaxation of strain is by generating interstitial dislocation loops at the interface. Elongated screw segments which have undergone little modification in shape are frequently observed.

For the alloy studied in this paper, the most frequently detected intergranular $(Cr,Mo,Fe)_{23}C_6$ carbides were formed by a discontinuous precipitation. In general, the grain boundaries appear to have one side which adheres to the particle interface, while the other is characterized by a serrated appearance. This is confirmed by electron diffraction which shows a parallel orientation between the cubic lattices of matrix and precipitate on one side of the boundary (Fig. 5). OM and TEM inspection (Figs. 3, 4a, and 6b) showed thick plate-like carbides growing on one side of the boundary. Carbide particles grow at the maximum rate in the direction of the boundary, forming plates which have edges parallel to (111) planes [7, 8]. During creep, precipitation of $M_{23}C_6$ is also known to occur on non-coherent twin boundaries at approximately the same time as on grain boundaries [7, 8]. The carbides formed within the grains have a preferred interfacial growth along (111)-$M_{23}C_6$ parallel to (111)-γ [7, 8]. Prolonged exposure to 800 °C induced a massive dissolution and coalescence of the $(Cr,Mo,Fe)_{23}C_6$ carbides which eventually formed a intergranular film morphology. This continuous film reduced both the effect of grain boundary pinning and the possibility of intergranular embrittlement [37–40].

Another important factor for the creep resistance of the investigated alloy is the presence of the γ' phase. After exposure to 700 °C, the volume fraction of the γ' phase is high enough to slightly improve the mechanical properties of the alloy. Comparing the microstructure of specimens 7C and 8C (from 700 to 800 °C), the γ' phase particles coarsened more than four-fold, from ~60 to 255 nm in diameter. Furthermore, at 800 °C, cubic rather than spherical particles were observed (compare Figs. 4 and 6). The differences observed in γ' particles were clearly a consequence of the higher-temperature exposure which both induced a partial coalescence in favor of the initially bigger particles and a re-dissolution of the initially smaller particles. The coalescence of γ'-particles in both specimens 7C and 8C was faster in the load-bearing regions of the crept specimens than in the head of the creep sample. This effect could possibly be interpreted as a stress-enhanced diffusion rate or as a dislocation-driven coarsening mechanism, which is also observed in other materials like steel [5–7, 12, 28, 34]. Moreover, the cubic γ' precipitates indicated that the γ'/γ interface might still be semi-coherent. However, the coarsened γ' phase still provided matrix strengthening by dislocation pinning in agreement with Dahotre and co-workers [41], as shown in Fig. 8.

The precipitation of γ' has been investigated in several Ni-based alloys. Recently, in an Ni–25Cr–20Co alloy with Mo, Nb, Ti, and Al addition [42, 43], precipitation has been observed at temperatures lower than 620 °C. Thermodynamic calculation on the same alloy indicated that γ' was not an equilibrium phase at temperatures between 821 and 1091 °C [43] and it was experimentally observed that higher temperatures (greater than 650 °C) favored a very fast coarsening of γ' that eventually transformed either into γ'' or orthorhombic δ. As a result, the alloy loses its strength, since the improvement in the yield strength is mainly due to the extensive precipitation of γ' although the γ'' and δ-phases have similar but weaker effects [32, 42–45].

In the investigated Ni–22Cr–12Co–9Mo alloy, exposure to 700 and 760 °C induced the precipitation of small amounts of fine rounded γ' particles. At 800 °C, these particles coarsened and took on a cubic-like shape although they were less abundant. At this temperature only a secondary improvement in the hardness of the material was observed.

Creep behavior

Some of the creep strength data available in literature for the Ni–22Cr–12Co–9Mo alloy are summarized in Fig. 9. Most of the data available refer to tests performed at 800 °C or higher temperatures. In Fig. 9 the initial applied stress is plotted versus the Larson Miller Parameter (LMP = $T(\log t + 20)$, where T is the test temperature expressed in Kelvin and t is the time to rupture, in hours).

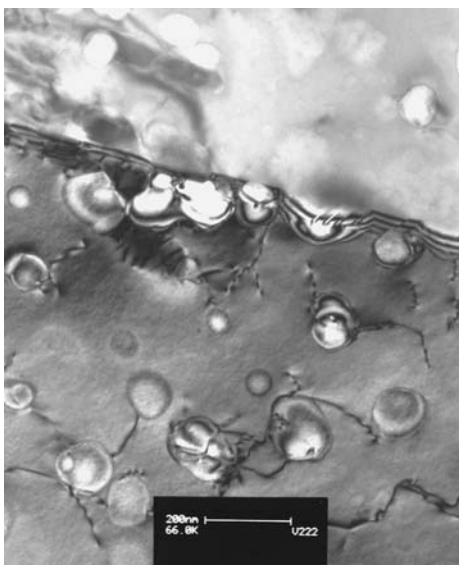

Fig. 8 BF-TEM of specimen 8C. Coarsened γ'-$Ni_3(Al,Ti)$ phase with sliding dislocations pinned and bounded

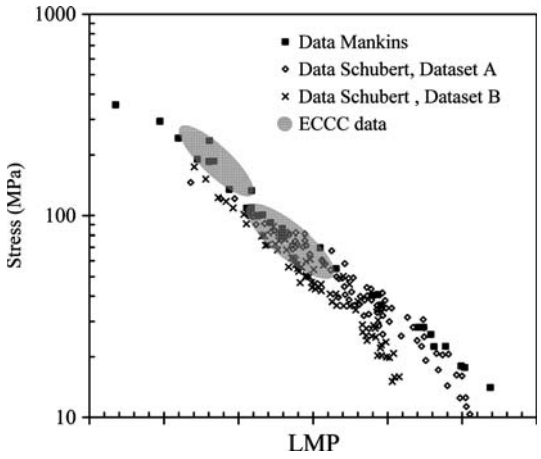

Fig. 9 Comparison between experimental (ECCC data) and literature creep data in terms of the Larson Miller Parameter. Experimental creep data at 800 °C are plotted using a *full circle* as a symbol while *open* and *full triangles* are the symbols used to represent, respectively, interruption and predicted rupture times at 700 °C. The stress versus LMP curve used to predict the creep rupture times of the investigated material is represented as a *continuous line*. Creep data results from Mankins et al. [11] are represented with *full squares*, while the results for the two heats reported by Schubert [44] are represented with *crosses* and *open diamond* symbols

More specifically, two sets of literature creep data (datasets A and B) have been proposed by Schubert et al. [46] which refer to creep tests performed at temperatures ranging from 800 to 1,000 °C. It can easily be seen in Fig. 9 that one of the two materials (dataset A) is more creep resistant at high-LMP values. Other creep results considered in the plot graph are those reported by Mankins et al. [13]. It is clear that at low LMP the creep properties reported by Mankins for the lowest test temperatures (700 °C or lower) tend to be better that those obtained from tests at higher-test temperatures.

The creep results for tests performed by a consortium of Italian Laboratories within the framework of a European Creep Collaborative Committee (ECCC), already published in [12], are also included in Fig. 9. It should be observed that creep rupture was reached only for creep tests carried out at 800 °C, while those which refer to 700 °C are only expected rupture times [12]. The same figure also shows the trend line used to define the experimental plan for ECCC tests [12], with which the rupture times at 800 °C are perfectly aligned. On the contrary, the rupture times estimated at 700 °C are about one order of magnitude longer than the predicted ones, related to a significant improvement in creep behavior at this test temperature. Therefore, creep strength data obtained at higher temperatures should be very carefully considered when extrapolating the creep strength of the alloy at 700 °C since the extrapolation could lead to a substantial underestimation of the creep life.

This can be correlated with the microstructural instability of the alloy in the investigated temperature range. As illustrated above, the microstructure of the Ni–22Cr–12Co–9Mo alloy changed at different creep temperatures with respect to the as-received condition. The main differences lie in the presence and distribution of carbides at grain boundaries, in the volume fraction and in the size both of the γ' phase and the δ-phase. The effects of these phases on creep properties have been previously presented and could explain the improved creep behavior of the alloy at 700 °C compared with 800 °C. The fraction and geometry of the γ'-phase precipitated at 700 °C contributed to an increase in the mechanical properties of the alloy, although its partial dissolution and coarsening severely reduced the strengthening effect of γ'-phases at 800 °C. Furthermore, exposure to 800 °C induces the coalescence of the $(Cr,Mo,Fe)_{23}C_6$ carbides in crept material . These carbides may eventually form an intergranular film morphology, which could modify grain boundary sliding conditions and the final fracture mechanism. Finally, the effect of the δ-phase, found only in specimens crept at 700 °C, is believed to contribute to the strengthening of the alloy, as has also been reported by other authors [47–50]. The specific zip-like morphology, starting from the grain boundary region and proceeding into the grain effectively pinned the sliding dislocations. The pinning effect is competitive compared with the effect of the fine square-shaped γ'-phase particles. The γ' pinning strength is believed to be lower due to its relatively low fraction compared with the δ-phase.

Conclusions

The microstructural evolution after different creep tests on an Ni–22Cr–12Co–9Mo alloy was characterized using TEM, SEM, and OM techniques. The microstructural investigations revealed the following main features:

1. In the as-received condition the material was characterized by a banded structure, which contained Cr- and Mo-carbides; this banded structure had fine grains yielding higher-hardness values compared with the surrounding coarser grained regions. More specifically, $M_{23}C_6$ carbides were always present, lying within the grain, on twins and along grain boundaries.
2. Creep exposure to 700 and 800 °C led to an extensive intragranular formation of γ'-$Ni_3(Al,Ti)$ precipitates. The size of these precipitates ranged between 60 and 255 nm depending on the test temperature. Their morphology was spherical at the lower test temperature and cubic at the higher-test temperature. This effect is consistent with the observed increase in the hardness of the material, with respect to the as-received material.

3. At 700 °C the δ-phase (Ni_3Mo) competitively formed with the γ'-$Ni_3(Al,Ti)$. The δ-phase started to form at the grain boundaries and proceeded in a zip-like path inwards. The presence of tangled sliding dislocations all around the plate-like δ-phase indicated that they are strengthening particles for the material. At 800 °C no trace of the δ-phase was found. Other precipitates observed were carbides such as $M_{23}C_6$—$(Cr,Co,Ni,Mo)_{23}C_6$ and, less frequently, MC—(Cr,Mo)C. The amount and morphology of these carbides changed with the exposure temperature. The Cr-, Mo- carbonitride CrMo(C,N) was rarely detected by microstructural inspections, while no MC, M_6C carbides were detected.
4. The microstructural instability of the alloy, in particular the large differences in size and distribution of γ'-precipitates at 700 and 800 °C, can account for the improved experimental creep resistance at 700 °C compared with expected creep life. This suggests that creep data obtained at the higher temperature should be very carefully considered when extrapolating the creep strength of the alloy at 700 °C, since they could lead to a substantial underestimation of the creep life.

Acknowledgements The authors are grateful to the other Italian creep laboratories, which contributed to the experimental creep test program (CESI (Piacenza, Milan), ISB (Milan) and CSM (Rome)). Thanks are also due to all the members of the WG3C of ECCC for their support and stimulating discussion.

References

1. Blum R, Vanstone RW (2005) ParsonS 2003, 1st Int. Conf. super-high strength steels, 2–4 Nov. 2005, Rome
2. Viswanathan R, Hanry JF, Tanzosh J, Stanko G, Schlingledecker J (2005) In: Shibli IA, Holdsworth SR, Merckling G (eds) Proc Conf. creep & fracture at high temperature components, 12–14 Sept. 2005, DEStech Publications, Lancaster, PA, p 59
3. Röster J, Götting M, Del Genovese D, Böttiger B, Kopp P, Wolske M, Shubert F, Pemkolla HJ, Seliga T, Thoma A, Sholz A, Berger C (2005) Adv Eng Mat 5:469
4. Donachie MJ, Donachie SJ (2002) Superalloys—a technical guide, 2nd edn. ASM International, Materials Park, OH, p 1
5. Martin U, Oetttel H, Mühle U, Jerenz M (2001) Adv Eng Mat 3:871
6. Cozar R, Pineau A (1973) Metall Mater Trans A4:47
7. Kegg CR, Silcock JM (1972) Scripta Metall 6:1083
8. Lewis MH, Hatterrsley B (1965) Acta Metall 13:1159
9. Loomis WT, Freeman JW, Sponseller DL (1964) Metall Mater Trans A67:714
10. Jones RD, Kapoor S (1973) J Iron Steel Inst 211:226
11. Peters DT (1967) Trans TMS-AIME 239:1981
12. Allen D, Keustermans JP, Grijbels S, Bicego V (2004) Mater High Temp 21:53
13. Mankins WL, Hoster JC, Bassford TH (1974) Metall Trans 5:2593
14. Rao GA, Prasad KS, Kumar M, Srinivas M, Sarma DS (2003) J Mater Sci Technol 19:1
15. Rao GA, Kumar M, Srinivas M, Sarma DS (2003) Mater Sci Eng A355:114
16. Lewis MH, Hattersley B (1965) Acta Metall 13:1159
17. Garzarotli F, Gerscha A, Francke FP (1969) Z Metallkunde 60:643
18. Sundararaman M, Mukhopadhyaya P, Benerjee S (1988) Mater Sci Forum 3:453
19. Shankar V, Shankara Rao KB, Mannan SL (2001) J Nucl Mater 288:222
20. Sun WR, Guo SR, Lee JH, Park NK, Yoo YS, Choe SJ, Hu ZQ (1998) Mater Sci Eng A247:173
21. Ferreire I, Stang RG (1983) Acta Metall 31:585
22. Merrick HF (1995) Metall Mater Trans A7:505
23. Valencia JJ, Spirko J, Schmees R (1997) In: Loria EA (ed) Superalloys 718, 625, 706 and various derivatives. TMS, Warredale, PA, p 753
24. Stoloff NS (1989) Int Mater Rev 34:153
25. Marquez C, Esparane GL, Koul AK (1989) Int J Powder Met 25:301
26. Maziasz PJ (1989) J Nucl Mater 169:95
27. Williams TM, Titchmarsh JM (1979) J Nucl Mater, 82:199
28. Williams TM, Titchmarsh JM (1981) J Nucl Mater 98:223
29. Chen W, Chaturvedi M (1993) Can Metall Quart 32(4):363
30. Campo E, Turco C, Catena V (1985) Metall Sci Tech, J. TEKSID, Italy, 3(1):16
31. Collins HE (1975) Metall Mater Trans 5:187
32. Kimball OF, Lai GY, Reynolds GH (1976) Metall Trans A 7:1951
33. Qiu YY (1996) J All Comp 232:254
34. Chen W, Chaturvedi M (1994) Mater Sci Eng A183:81
35. Xue H, Lijun W, Hui X, Runguang L, Shaogang W, Zhonglin C (2003) J Mater Proc Techn 137:17
36. Betteridge W, Franklin AW (1957) J Inst Met 85:473
37. Devine TM (1990) Corrosion Sci 30:135
38. Mathew MD, Sasikala G, Bhanu Sankara Rao K, Mannan SL (1991) Mater Sci Eng A148:253
39. Iacoviello F, Casari F, Gialanella F (2005) Corros Sci 47:909
40. Park C-J, Ahn M-K, Kwon H-S (2006) Mater Sci Eng A418:211
41. Dahotre NB, McCay MH, McCay TD, Hubbard CR, Porter WD, Cavin OB (1993) Scripta Metall Mater 28:1359
42. Evans ND, Maziasz PJ, Swindeman RW, Smith GD (2004) Scripta Mater 51:503
43. Zhao S, Xie X, Smith GD, Patel SJ (2003) Mater Sci Eng A355:96
44. Kindrachuk V, Wanderka N, Banhart J (2006) Mater Sci Eng A417:82
45. Murakumo T, Kobayashi T, Koizumi Y, Harada H (2004) Acta Mater 52:3737
46. Shubert F, Bruch U, Cook R, Diehl H, Ennis PJ, Jakobeit W, Penkalla E, Ullrich G (1984) Nucl Technol 66:227
47. Rai SK, Kumar A, Shankar V, Jayakurmar T, Rao KBS, Raj B (2004) Scripta Mater 51:59
48. Yuan H, Liu WC (2005) Mater Sci Eng A408:281
49. Liu L, Zhai C, Lu C, Ding W, Hirose A, Kobayashi KF (2005) Corros Sci 47:255
50. Azadian S, Wei L-Y, Warren R (2004) Mater Charact 53:7